PCCP

PAPER

View Article Online
View Journal | View Issue

Cite this: *Phys. Chem. Chem. Phys.*, 2015, **17**, 15131

Gold atomic clusters extracting the valence electrons to shield the carbon monoxide passivation on near-monolayer core–shell nanocatalysts in methanol oxidation reactions†

Tsan-Yao Chen,*[ab] Hong Dao Li,[c] Guo-Wei Lee,[c] Po-Chun Huang,[a] Po-Wei Yang,[a] Yu-Ting Liu,[d] Yen-Fa Liao,[e] Horng-Tay Jeng,[c] Deng-Sung Lin[c] and Tsang-Lang Lin[a]

Received 23rd February 2015,
Accepted 7th May 2015

DOI: 10.1039/c5cp01103e

www.rsc.org/pccp

Atomic-scale gold clusters were intercalated at the inter-facet corner sites of Pt-shell Ru-core nanocatalysts with near-monolayer shell thickness. We demonstrated that these unique clusters could serve as a drain of valence electrons in the kink region of the core–shell heterojunction. As jointly revealed by density functional theory calculations and valence band spectra, these Au clusters extract core-level electrons to the valence band. They prevent corrosion due to protonation and enhance the tolerance of CO by increasing the electronegativity at the outermost surface of the NCs during the methanol oxidation reaction (MOR). In these circumstances, the retained current density of Pt-shell Ru-core NCs is doubled in a long-term (2 hours) MOR at a fixed voltage (0.5 V *vs.* SCE) by intercalating these sub-nanometer gold clusters. Such novel structural confinement provides a possible strategy for developing direct-methanol fuel cell (DMFC) modules with high power and stability.

Introduction

The structural and chemical stability of electrocatalysts in long-term methanol oxidation reactions (MOR) is the dominant factor in developing durable direct-methanol fuel cells (DMFCs) anodes with high performance. From the standpoint of heterogeneous interfaces, this target can be achieved by growing nanocatalysts (NCs) with highly stressed intra-particle heterojunction confinements. Binary and ternary metallic systems in different structural configurations (*i.e.*, alloy, cluster-in-cluster, and core–shell structures) were extensively studied for the stabilization of NCs. Among these structures, core–shell NCs exhibit the most convincing structural stability across all dimensional regimes. Such unique structures can be developed by depositing methanol-active atoms onto selected core crystallites in monolayer thickness while retaining compressive lattice strain in the shell region.

From the standpoint of heterogeneous crystal growth, a core–shell structure is the simplest platform for manipulation of lattice strain and composition in the near-surface region in binary NCs. Such a structure has normally been developed by properly selecting the identity of core and shell crystallites with precision control of the shell thickness.[1] State-of-the-art studies on core–shell NCs demonstrated outstanding electrochemical durability in a DMFC test above 10^5 cycles and CO oxidation activity in a fuel reformate system at room temperature.[2–4] These experimental results were subsequently confirmed by density functional theory (DFT) calculations. By combining experimental and theoretical results, the heterogeneous catalytic activity of core–shell NCs is mainly determined by the top layers of shell atoms (about 4–5 Å depth in most cases).[5,6] These implications promised the design of new NCs in frontier green energy devices.[6] However, their electrochemical properties (*i.e.*, activity, selectivity, and stability) remain to be improved for applications at industrial production scales.

To meet standards for industrial applications, the structure and performance durability of NCs, particularly in long-term redox reactions in operational devices, are of essential importance. These crucial factors can be improved by increasing the extent of heteroatomic mixing while retaining the densities of surface-active sites and the lattice strain in the near-surface region of NCs. Our previous studies and the literature demonstrated

[a] *Department of Engineering and System Science, National Tsing Hua University, Hsinchu 30013, Taiwan. E-mail: chencaeser@gmail.com; Fax: +886 3 5728445; Tel: +886 3 5742671*
[b] *Institute of Nuclear Engineering and Science, Hsinchu 30013, Taiwan. E-mail: chencaeser@gmail.com; Fax: +886 3 5728445; Tel: +886 3 5742671*
[c] *Department of Physics, National Tsing Hua University, Hsinchu 30013, Taiwan. E-mail: dengsunglin@gmail.com*
[d] *Department of Environmental Science and Engineering, Tunghai University, Taichung 40704, Taiwan. E-mail: ytliu@thu.edu.tw*
[e] *National Synchrotron Radiation Research Center, Hsinchu 30013, Taiwan*

† Electronic supplementary information (ESI) available: The DFT simulation, XAS, XPS, and TEM results are enclosed. See DOI: 10.1039/c5cp01103e

that the chemical stability of NCs in electrochemical devices (in the methanol oxidation reaction (MOR) in fixed-voltage anode and fuel cell voltage cycle tests) strongly depended on intra-crystallite geometrical confinements. Among binary systems in different configurations, core–shell-structured NCs display the highest extent of heteroatomic mixing, lattice strain, and interface conjunction. These features promote electron injection and heteroatomic mixing (hybridization) and thus significantly enhance the chemical activity (selectivity) and structural stability (including resistance to protonation corrosion and CO poisoning) at the reaction sites in NCs.[3]

In this study, binary NCs comprising a Pt shell of 1.5 atomic layers and a 2.8 nm Ru core were synthesized. To further enhance the physicochemical stability of NCs, gold clusters of sub-nanometer size were intercalated at the inter-facet corner sites on the Pt shell. We demonstrate that these gold clusters trigger electron injection from core to shell regions. This concentrates negative charges in corner regions, thus ejecting negatively charged anions (CO molecules) from the NCs surface. In these circumstances, the retained current density of Pt-shell Ru-core NCs is doubled in a long-term MOR test at 0.5 V after 2 hours by inserting these atomic-scale gold clusters. Such novel structural confinement provides a possible strategy for developing modules with high power and stability in a direct-methanol fuel cell (DMFC). Details of the heteroatomic restructuring of NCs in relation to electrochemical performance in the MOR will be given in later sections. In addition, we will clarify how the structural stability of core–shell-structure NCs is further enhanced *via* intercalation of Au clusters in their corner regions. To attain our target, small-angle X-ray scattering (SAXS), high-resolution transmission electron microscopy, X-ray absorption, and density functional theory simulations were employed in a complementary way.

Experiment

The atomic structure of experimental NCs was controlled by using sequential designed polyol reduction.[7] The average particle size, size distribution, and geometrical configuration of these NCs were determined by small-angle X-ray scattering analysis. The impact of the intercalation of Au clusters on the atomic arrangement and CO sorption processes of NCs were simulated using *ab initio* density functional theory (DFT) calculations. The valence band structure was elucidated by UPS spectroscopy. Combining these structure results, the impacts of the intercalation of Au clusters on the activity and structural stability of NCs were jointly resolved *via* fixed-voltage long-term MOR analysis. Details of sample preparation, structure interpretations, and discussions are given in the following sections and the ESI.†

Materials

Metal precursors (including hexachloroplatinic acid ($H_2PtCl_6{\cdot}6H_2O$, 99 at%), hydrogen tetrachloroaurate(III) hydrate ($HAuCl_4$, ACS reagent >49%), and ruthenium(III) chloride hydrate ($RuCl_3{\cdot}3H_2O$, 99.0%)) and polymer stabilizers (polyvinylpyrrolidone) stabilizer (PVP-40, MW ~42 000, 99%) were obtained from Sigma-Aldrich. H_2SO_4 (99.9%) and HNO_3 (99.9%) were obtained from Sigma-Aldrich. The reaction solvent (ethylene glycol, EG > 99.5%) was obtained from Fluka Co. Inc.

Catalyst preparation

Ru_{Core}–Pt_{Shell} NCs (denoted as PtS/RuC) were synthesized by a two-step polyol method with the reaction sequences in conformity with the expected atomic architecture. Firstly, hcp Ru cores with an average diameter of ~2.5 nm were prepared by reducing 100 mM ruthenium chloride in ethylene glycol (EG) *via* thermal treatment, as shown in our previous work.[8] Secondly, a Pt shell of near-atomic monolayer thickness was produced based on a heterogeneous nucleation and growth pathway by thermal reduction of Pt anions ($H_2PtCl_6{\cdot}6H_2O$, 99 at%) on the surface of a Ru core in the presence of 10 wt% polyvinylpyrrolidone (PVP) stabilizer in EG at 160 °C for 2 h. The shell thickness was controlled by adjusting the Pt/Ru ratio to 1.5. The intercalation of sub-nanometer gold clusters at the corner sites of PtS/RuC NCs was achieved by reducing gold cations (in an atomic ratio of Au/Pt = 0.1) in the subsequent polyol reactions. In this step, the surface sites of NCs served as nuclei for catalysing the heterogeneous crystal growth of Au and the resulting NCs are denoted as Au@PtS/RuC.

Catalyst characterizations and methanol oxidation reaction in long-term testing

The microstructure of NCs was elucidated by conventional and high-resolution transmission electron microscopy (HRTEM). The nanostructure and crystal structure parameters of NCs were determined by SAXS and XRD at the beamlines **BL-23A** at NSRRC (Taiwan) and **BL-12B2** at Spring-8 (Japan), respectively. The valence band spectrum of the NCs was collected at the beamline **BL-24A1** at NSRRC. The electrochemical stability of the NCs, which was correlated to their surface composition and structures, was determined by fixed-voltage long-term MOR reaction analysis (CH Instruments Model 600B). The electrochemical cell for CV analysis consisted of a working electrode, an SCE reference electrode, and a 10 mm × 10 mm platinum foil counter electrode. Details of the characterization methods and instrumental parameters are given in ESI.†

Density functional theory simulations

Theoretical analysis of first-principles calculations and analysis was performed using the Vienna *ab initio* simulation package (VASP) based on density functional theory (DFT). Projector augmented-wave (PAW) potentials were used to describe the core electrons. A generalized gradient approximation (GGA) in the form of the Perdew–Burke–Ernzerhof (PBE) functional was adopted to describe the exchange correlation functional, which was developed for the calculation of the surface system. The Pt supercell was simulated using a repeating 6 × 6 slab model, in which 1.5 atomic layers of Pt atoms (packing in (111) facet symmetry), 4 layers of Ru atoms (in (110) facet symmetry) as a sub-layer slab, and 5 Au atoms as a cluster intercalated at the corner sites. In these calculations, the vacuum region was set to 30 Å, minimizing potential interference between the top and bottom surfaces of the periodic slabs. In brief, the periodic slab

comprises four layers of Ru, one and a half layers of Pt atoms, and a vacuum layer of 30 Å, where CO molecules were located at the corner sites of the top surface. A kinetic energy cut-off of 300 eV for the plane-wave basis was used. Finally, the cut-off plane-wave expansion was taken to be 300 eV and the Monkhorst–Pack mesh of *k*-points for the irreducible Brillouin zone (IBZ) was chosen to be $6 \times 6 \times 1$. The structure was optimized until the energy and net force on every atom were smaller than 10^{-5} eV and 0.025 eV $Å^{-1}$, respectively.

Results and discussions

Nanostructure of the nanocrystallite

The nanostructure (including the particle shape, average particle size (D_{avg}), surface configurations, and crystal structure) of the NCs was elucidated using high-resolution transmission electron microscopy (HRTEM). Bright and dark-field HRTEM images of PtS/RuC and Au@PtS/RuC NCs are shown in Fig. 1. As shown in Fig. 1a, PtS/RuC has grown into a multifaceted crystallite with preferential orientation at (111) facets exposed to the surface in different directions (indicated by the arrows in red). These NCs are disk-like in shape and are grown by locating Pt atoms onto the Ru(0001) facet, where twin boundaries (denoted by the white dashed lines in bright and dark-field images) in inter-facet regions indicate the formation of semi-coherent interfaces. Here, the inter-planar spacing is determined to be 2.172 Å, which is reduced by about 3.9% compared to that of the Pt(111) facet in metallic Pt (~2.262 Å). Such lattice compression is triggered by locating a crystal with large lattice space (Pt(111) facets) onto a substrate with small lattice space (Ru(0001) facets). In addition, this lattice compression is applied in a lateral direction in the near-surface region. In the case of Au@PtS/RuC (Fig. 1b), the lattice spacing at twin facets is determined to be 2.351 Å.

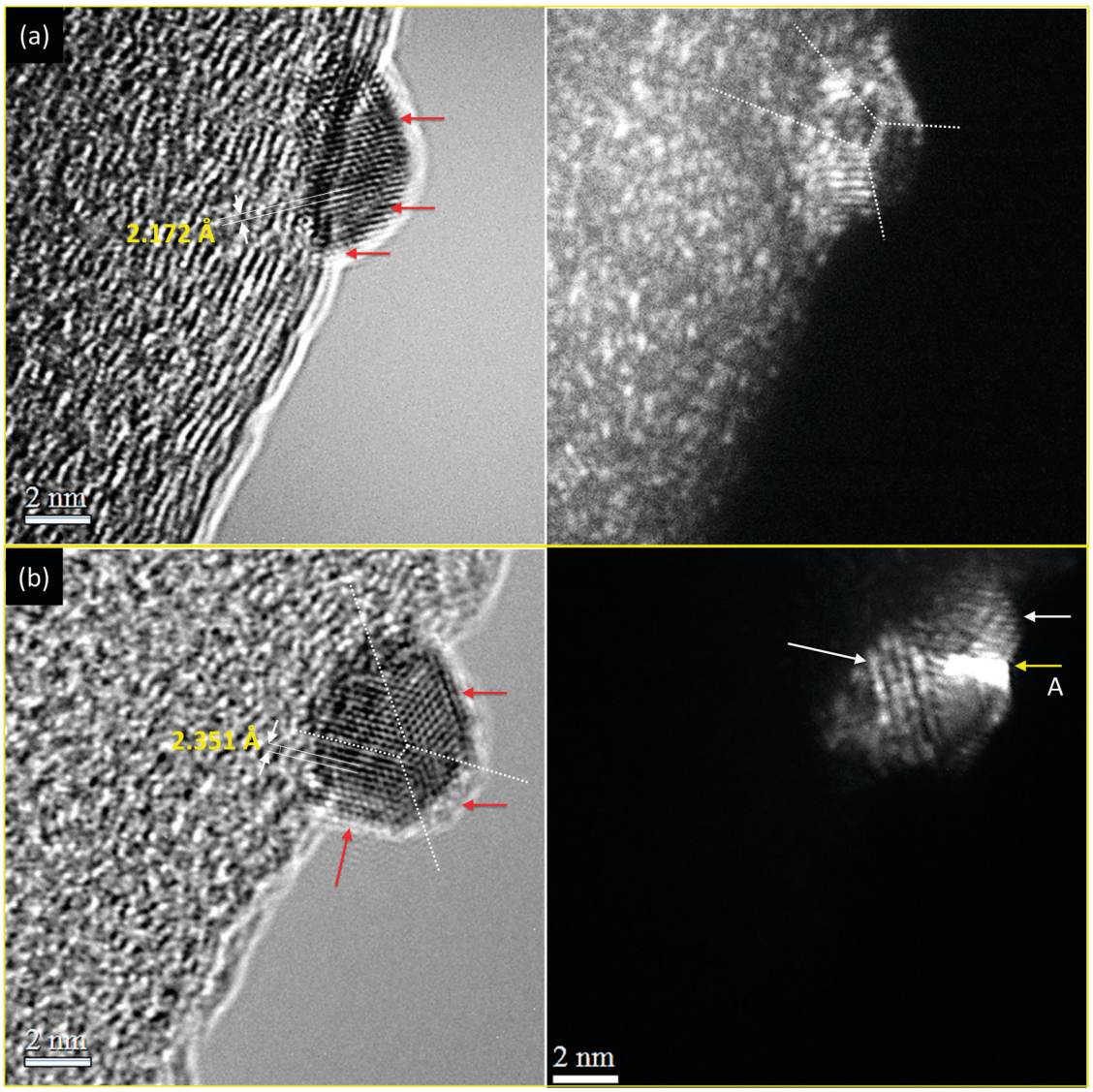

Fig. 1 Bright and dark-field high-resolution transmission electron microscopy (HRTEM) images of (a) PtS/RuC and (b) Au@PtS/RuC, wherein NCs were dispersed on a glassy carbon grid.

This suggests that Au atoms are possibly grown on (111) facets of Pt or at edge sites of a PtS/RuC nanodisk.[9] Given that Au crystals possess higher surface energy than that of Pt, these Au clusters would tend to grow as plateaus that truncate the corner sites to form additional (111) facets at the corner sites of PtS/RuC (see Fig. S1, ESI†) *via* a transmetallation reaction $2Au^{3+} + Pt^{M} \rightarrow 2Au^{M} + Pt^{6+}$, followed by reduction of Au^{3+} at heterogeneous nuclei (Au^{M}) upon interacting with CH_3CHO: radicals.[3,6,10,11] The formation of Au clusters and transmetallation-induced crystal truncation are further revealed by dark-field HRTEM at a tilted angle (Fig. 1b, left). As indicated, the prevalent bright spheres (indicated by solid arrows in white) resemble atoms with strong electron refraction in an ordered arrangement with (111) atomic packing geometry in different orientations exposed to the NCs surface. The arrow A in yellow denotes the presence of a surface stage. This asymmetric crystal shape cannot be formed *via* homogeneous crystal growth pathways and is thus a direct indication of the growth of external crystal clusters at inter-facet corner axis sites.

The results of HRTEM outline a steric scattering model for refining the structural parameters of core–shell-structured NCs (including D_{avg}, Schulz distribution of particle size (P_R), and shell thickness (T_S)) in SAXS analysis. In this work, the particle shape and sequences of crystal growth for each component are taken into account in building these models. SAXS spectra [$I(Q)$ *vs.* Q] and the corresponding Schulz distributions of particle size are shown in Fig. 2a and b, respectively. The features of the SAXS spectra comprise the interferences of incident X-ray photons that are scattered between the inter-particle clusters (*i.e.*, the structure factor $F(Q)$ for $Q < 0.07$ Å^{-1}) and intra-particle interfaces of the NPs (the form factor $P(Q)$ for $Q > 0.07$ Å^{-1}). For PtS/RuC, the SAXS spectrum can be described by combining the contributions of fractal aggregate and core–shell cylindrical models (see eqn (1) for PtS/RuC and eqn (2) for Au@PtS/RuC).[12–14]

$$I(Q) = A^{F}S(Q)^{F}P(Q)^{F} + A^{CS\_C}S(Q)^{CS\_C}P(Q)^{CS\_C} \quad (1)$$

$$I(Q) = A^{Fclu}S(Q)^{Fclu}P(Q)^{Fclu} + A^{CS\_C}S(Q)^{CS\_C}P(Q)^{CS\_C} \quad (2)$$

In eqn (1), A is the number density of the scattering objects. Both $S(Q)$ and $P(Q)$ are functions of the momentum transfer (Q) between incident and scattered X-rays. Q is given by $Q = (4\pi/\lambda) \times \sin(\theta/2)$ in an elastic scattering process, where θ denotes the angle between the incident and scattered beams at a wavelength of λ. The superscripts F (fractal) and CS_C (core–shell cylinder) refer to the model the parameters belong to. In the case of Au@PtS/RuC, incident X-rays will be scattered between the Au clusters and at the intra-particle surface (indicated by arrow X) where a scattering scheme of a model of Au clusters on a core–shell cylinder particle is shown in Fig. 2c. Scattered X-rays at Au clusters on core–shell NPs contribute to diffuse background scattering (denoted by arrows Y), whereas inter-particle scattering correlation factors (A^F, $S(Q)^F$, and $P(Q)^F$) are replaced by inter-cluster factors, which are represented by A^{Fclu}, $S(Q)^{Fclu}$, and $P(Q)^{Fclu}$ (see eqn (2)). The corresponding fitting curves are shown in Fig. 2a. As clearly depicted, for PtS/RuC NCs the least-squares fitting curves of the proposed model fit the SAXS spectrum well

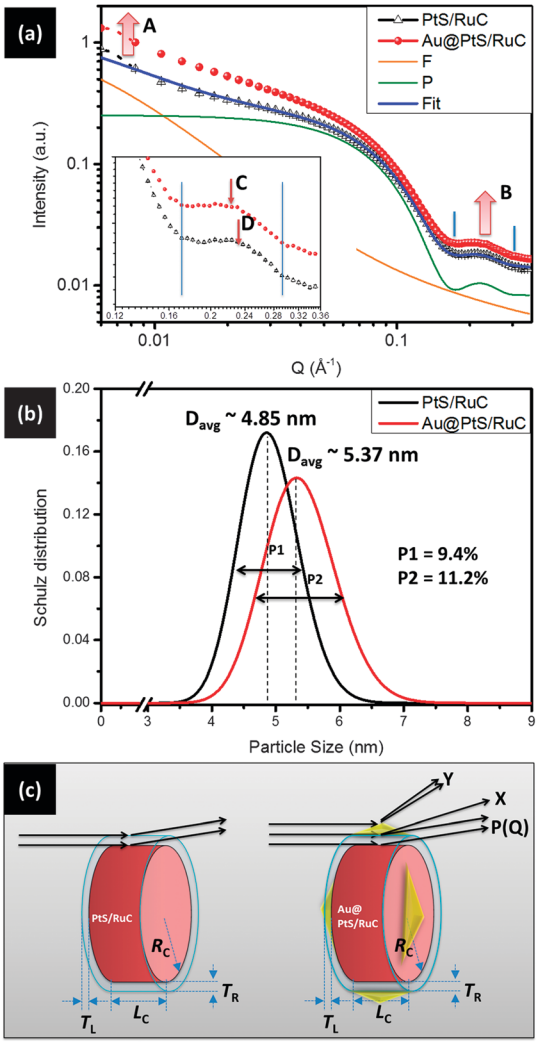

Fig. 2 (a) Small-angle X-ray scattering spectra; where inset demonstrates the magnified spectra around the scattering hump B, (b) Schulz particle size distribution, and (c) scattering contributions of the proposed binary structural models to fit the experimental SAXS spectra.

(the fitting curves for all samples are given in Fig. S2, ESI†). The broadening and downshift of the hump in the $F(Q)$ oscillation (from D to C) indicate the increasing phase divergence (caused by X-ray scattering at the high-roughness surface (arrow Y) and the Au–Pt interface, arrow X) and length of the interference cavity (the distance between the inner and outer boundaries of core–shell NCs, T_S) in the presence of Au intercalations. The geometrical scattering effects of Au clusters were further revealed by comparing the P_R and D_{avg} of the two NCs. As shown in Fig. 2b, the D_{avg} of PtS/RuC is determined to be 4.85 nm with a P_R of 9.4%, which suggests definite particle size distributions and uniform T_S. For Au@PtS/RuC the D_{avg} is determined to be 5.37 nm, which is about 2.0 atomic layers thicker than that of PtS/RuC. Considering the input Au/Pt ratio, this value seems controversial; however, it can be explained by a model of heterogeneous thin-film growth with slight layer-plus-island (Stranski–Krastanov (SK) mode) growth at inter-facet corner sites. This phenomenon is consistently demonstrated by the scattering model in Fig. 2c. In this case,

Table 1 Structural parameters of PtS/RuC and Au@PtS/RuC NCs determined by fitting the corresponding SAXS spectra using binary models, which comprise polydispersed core–shell cylinder and fractal components

NCs[a]	D_{avg} (nm)	R_C (nm)	L_C (nm)	T_R (nm)	T_L (nm)	P_R (%)	D^{clu} (nm)
PtS/RuC	4.85	1.54	2.45	0.83	0.49	9.4	
Au@PtS/RuC	5.37	1.48	2.83	0.75	0.51	11.2	0.5

[a] D_{avg}, R_C, L_C, T_R, T_L, P_R, and D^{clu} denote the average particle size, radius on the radial side, length on the facial side, shell thickness on the radial side, shell thickness on the facial side, Schulz distribution of particle size, and diameter of clusters, respectively.

scattered X-rays will be diffused by the discontinuous interfaces between Au clusters, thus resulting in an increase in P_R to 11.2%.

The impacts of Au clusters on the structural parameters of core–shell cylinder NCs (including the mean core radius R_C, core length L_C, and corresponding crystal shell thicknesses T_R and T_L on their surfaces, respectively) were quantitatively derived by model analysis and the results are summarized in Table 1. As shown, PtS/RuC comprises a thin-shell crystal with T_R = 0.83 nm and T_L = 0.49 nm on facial (with a diameter ($R_C \times 2$) of 3.08 nm) and radial (with a L_C of 2.45 nm) axes, respectively. A slight increase in L_C accompanied by a reduction in T_R is found for Au@PtS/RuC. This feature corresponds to preferential spontaneous transmetallation on the radial surface (where a high density of surface defects is prevalent) compared to the facial surface on nanodisk NCs. Hence, defects on the zone axes of the facets (*i.e.*, corners) act as nucleation sites for locating Au clusters (at a size of ~0.5–0.6 nm).[10,15] As also revealed by HRTEM, the growth of these discrete Au clusters truncate the PtS/RuC corners and create small close-packed facets.

Valence band structures of the nanocrystallite

Valence band electrons are the direct mediators driving catalytic interactions (*i.e.*, the chemisorption/ejection of reagent/product molecules onto/from active reaction sites) on NCs. Their distributions are dominated by the heteroatomic mixture, surface atomic arrangements, defect density, and types of heterojunction in the near-surface regions. From the standpoint of heterogeneous catalysis, surface defects (for instance, kinks/steps and corner sites) pose dilemmas for the performance of NCs. On the positive side, prevalent defects with dangling bonds are sites with high surface free energy that enable redox reactions in pathways with low activation energy. However, on the negative side, regions that are deficient in interatomic bonding support are both chemically (tend to be poisoned by chemisorbed molecules) and mechanically unstable (tend to relocate into clusters on reducing the surface free energy). The intercalation of Au clusters adds a localized heterojunction to PtS/RuC. This not only reinforces defect sites against restructuring but also creates a strong negatively charged dipole field for shielding neighbouring Pt atoms from chemical poisoning. These proposed shielding effects are consistently demonstrated by valence band photoemission spectroscopy (VB). VB spectra of PtS/RuC and Au@PtS/RuC are compared in Fig. 3. As clearly shown, the VB of NCs comprises several regions: (A) a steep area ranging from 0.00 to 0.75 eV, a slope with an inflection point

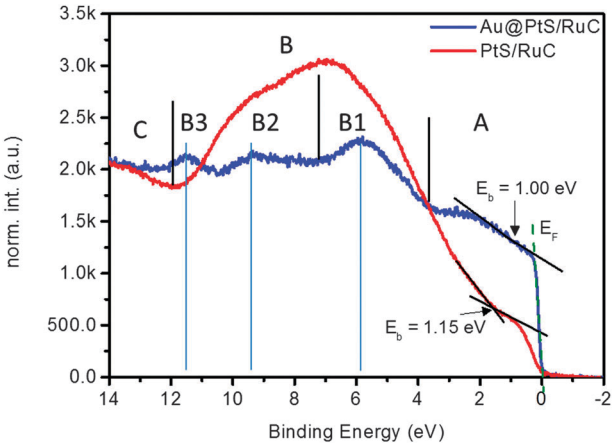

Fig. 3 Valence band spectra of PtS/RuC and Au@PtS/RuC NCs.

at 1.15 eV (*i.e.*, the surface binding energy, E_b), and a second rise with a steep slope to 3.41 eV; (B) a broad band from 3.41 to 11.78 eV (centred at ~6.9 eV); and (C) a valley centred at 12.3 eV. In comparison with VB spectra of Ru and Pt NCs, because substantial modifications in the VB features are found, the obtained spectrum should not be regarded as the sum of their individual contributions. Instead, it resembles hybridization of the crystal sub-layer (in our study, Ru-core NCs) with the VB structures of the crystal outer shell (Pt). Given that the intensity of the VB below the Fermi level is normalized to be the same, the substantially attenuated intensity (region A) indicates prevalent empty states (a significantly decreased density of states, DOS) in the outermost band. Such open valence states are caused by heterojunction-controlled relocation of charge (local charge injection) from Pt to the sub-layer crystal core and chemisorption of oxygen.[4,9] The broad hump with high intensity in region B could be attributed mainly to compression of the valence band in combination with a certain amount of oxidation in the Pt crystal. These valence band structures, based on DFT predictions in the literature, tend to accept electrons from chemisorbed molecules and therefore facilitate the initial MOR current of PtS/RuC (results are given in the later sections). Region C resembles near-core-level photoemission signals, where dramatically increased emission intensity is found at binding energies above 11.8 eV (extended VB spectra are shown in Fig. S3, ESI†). Compared to that of PtS/RuC, a quantum leap in photoemission intensity is found in region A. Such novel characteristics resemble the preservation of valence charge on the particle surface by the localized heterojunction around the Au clusters on the Pt-shell crystallite. As demonstrated by our DFT simulations (Fig. S4 and Table S1, ESI†), these negatively charged domains (Au intercalations) together with the sub-layer charge injection band weaken the chemisorption of anionic species (oxygen in our case) and thus protect the particle surface from oxidation. Such weakening coincides with reduced surface E_b (~0.95–1.00 eV) compared to that of PtS/RuC. In the high binding energy region (region B), the bandwidth is expanded to 12.3 eV and split into B1, B2, and B3 centred at 6.1, 9.3, and 11.6 eV, respectively. The centres of these distinct band features coincide with those of a metallic Pt crystallite at various facets. In addition, compared to the bands of

Pt metal with surface oxidation (Fig. S3, ESI†), the upshift in energy and modifications in shape of these split bands again prove the occurrence of anti-oxidation shielding of Au clusters on the Pt shell. With such shielding, the resistance to corrosion due to protonation, surface oxidation, and CO poisoning of PtS/RuC will be substantially improved. These hypotheses are proved by combining the results of DFT simulations (Fig. S4, ESI†), X-ray absorption spectroscopy analysis (Fig. S5, ESI†), and long-term MOR testing.

Au clusters shielding CO chemisorption

Based on heterogeneous crystal growth theory and the results of structural analyses, we note that Au clusters tend to intercalate at the inter-facet corners of PtS/RuC. These clusters protect the most active sites from direct interaction with carbonaceous inhibitors (*i.e.*, CHO and CO ligands) and therefore substantially enhance the MOR activity of NCs in long-term operation.

Such a hypothesis was proved *via ab initio* DFT simulations. In our work, five close-packed Au atoms were located onto the kink region as a cluster that intercalates at Pt on a Ru heterojunction slab (one and a half layers of Pt atoms on four sublayers of Ru(110) facets) for simulating the shielding effects on the CO bonding energy at PtS/RuC NCs. On the PtS/RuC substrate, these Au atoms (yellow spheres) are close-packed in the kink region of the Pt shell (Fig. S4, ESI†). It is important to note that the heteroatomic bond length (Table S2, ESI†) at the interface (*i.e.*, Pt1–Au1 and Pt2–Au2) is determined to be 2.852 ± 0.08 Å. This value is ~0.07 Å longer than that of the homoatomic Pt–Pt bond distance (~2.779 ± 0.06 Å), which is an indication of the preferential clustering of Au atoms by minimizing the surface free energy.[6] Consequently, local lattice compression in the Pt shell adjacent to the Au cluster due to a lattice mismatch can be expected. As consistently revealed by Pt and Au 4f core-level XPS (Fig. S6 and Table S3, ESI†) and VB spectra (Fig. 3), this strain and an electronegative dipole extract electrons from the Pt shell to the Au cluster. They create a negatively charged field and thus protect the Pt shell from oxidation and CO poisoning at the Au@PtS/RuC surface. DFT simulation results consistently demonstrate these impacts of electron relocation on the chemisorption behaviour of electronegative sorbates (*i.e.*, O ligands and CO molecules) on NCs. Simulation models (comprising a CO molecule at a bridge site on the top layer or edge of the Pt shell and a bridge site on the Au cluster) with their sorption energies are shown in Fig. 4 (the structural parameters are summarized in Table S2, ESI†). As illustrated, the sorption energy of CO at bottom bridge sites (where CO is located onto the surface of one monolayer of Pt on a Ru(0001) facet) is determined to be ~1.13 eV, which is a consistent result with that found in the literature.[3,5] The sorption energies at bridge sites on the top layer (with 1.5 monolayers of Pt on Ru(0001)) and at the edge are found to be higher than expected (the value should be between 1.13 (1.0 layer) and 1.33 eV (2.0 layers)). Such a controversial result could be rationalized by the occurrence of strong chemisorption that eliminated the defect density in order to minimize the surface energy. In these circumstances, the CO sorption energy at edge Pt–Pt bridge sites (**Pt(Pt)E_b**) is ~0.14 eV higher than that at top-layer sites (**Pt(Pt)_b** −1.97 eV), which resembles the CO sorption preference in PtS/RuC. In the case of Au@PtS/RuC, a similar preference can be expected. However, compared to **Pt(Pt)E_b**, it is surprising to note that the sorption energy is substantially increased by ~0.41 eV (−1.53 eV) at Pt–Pt bridge sites adjacent to Au clusters (**Pt(Au)_b**) and even higher energy (−0.62 eV) is found at Au–Au bridge sites on a Au cluster (**Au(Au)_b**). These results are convincing demonstrations of the reinforcement of chemical stability in PtS/RuC by intercalation of Au during the MOR in long-term testing. Combining the results of band structure simulation and VB spectra, such CO shielding effects could be attributed to electron extraction from the Ru core and the Pt shell to Au clusters *via* a localized strain field at the heterojunction. In this case, Au@PtS/RuC possesses prevalent charged domains for ejecting anionic ligands (OH: or O:) or electronegative molecules (*e.g.*, CO) from its surface.

Catalyst MOR stability

The stability of NCs was investigated *via* chronoamperometric analysis (typically named as AC analysis) in a long-term MOR.

Current–time curves for MWCNT-supported PtS/RuC and Au@PtS/RuC NCs in the MOR at a fixed applied voltage (0.5 V *vs.* SCE) are shown in Fig. 5. Three current regions A, B, and C are found on the AC curve, which correspond to changes in current density due to surface atomic restructuring, an imbalance in redox electrochemical kinetics, and CO poisoning, respectively. As illustrated, the initial current density of PtS/RuC NCs is determined to be ~225 mA cm^{-2} mg^{-1}, which is ~150% higher than that of Au@PtS/RuC (~92 mA cm^{-2} mg^{-1}). Compared to PtS/RuC, the electrochemical surface area of Au@PtS/RuC is reduced by only ~11%. Hence, such an abnormal drop in current could mainly be attributed to the suppression of methanol chemisorption kinetics due to the presence of a negatively charged field around Au intercalations, instead of geometric capping effects. In region A, the MOR activity of PtS/RuC NCs exponentially decayed by 78% in the first 15 min. The high rate of drop in current can be rationalized by competition between hydroxide (OH^-) ligands and reactants (methanol in this case). These OH ligands form an electrostatic double layer (EDL), which hinders the subsequent chemisorption of methanol and therefore suppresses the MOR current of PtS/RuC.[16,17] However, the drop in current in region A is reduced to ~30% on the AC of Au@PtS/RuC. This reveals the shielding effects of the Au clusters at the most reactive corner sites from OH ligands. Once the competition between the sorption kinetics of MeOH molecules and that of OH ligands reaches a metastable thermodynamic balance (indicated by arrow X for PtS/RuC), the subsequent stability of the reaction activity (current density in region B) is dominated by the atomic structure on the NCs. After the reaction time passes the X node, an inversion point in the AC current variation is found, which implies a certain extent of atomic restructuring caused by protonation corrosion on PtS/RuC. This corrosion is facilitated by surface oxidation at Pt corner sites and is inevitable unless the structure of NCs is protected. On the other hand, no inversion point

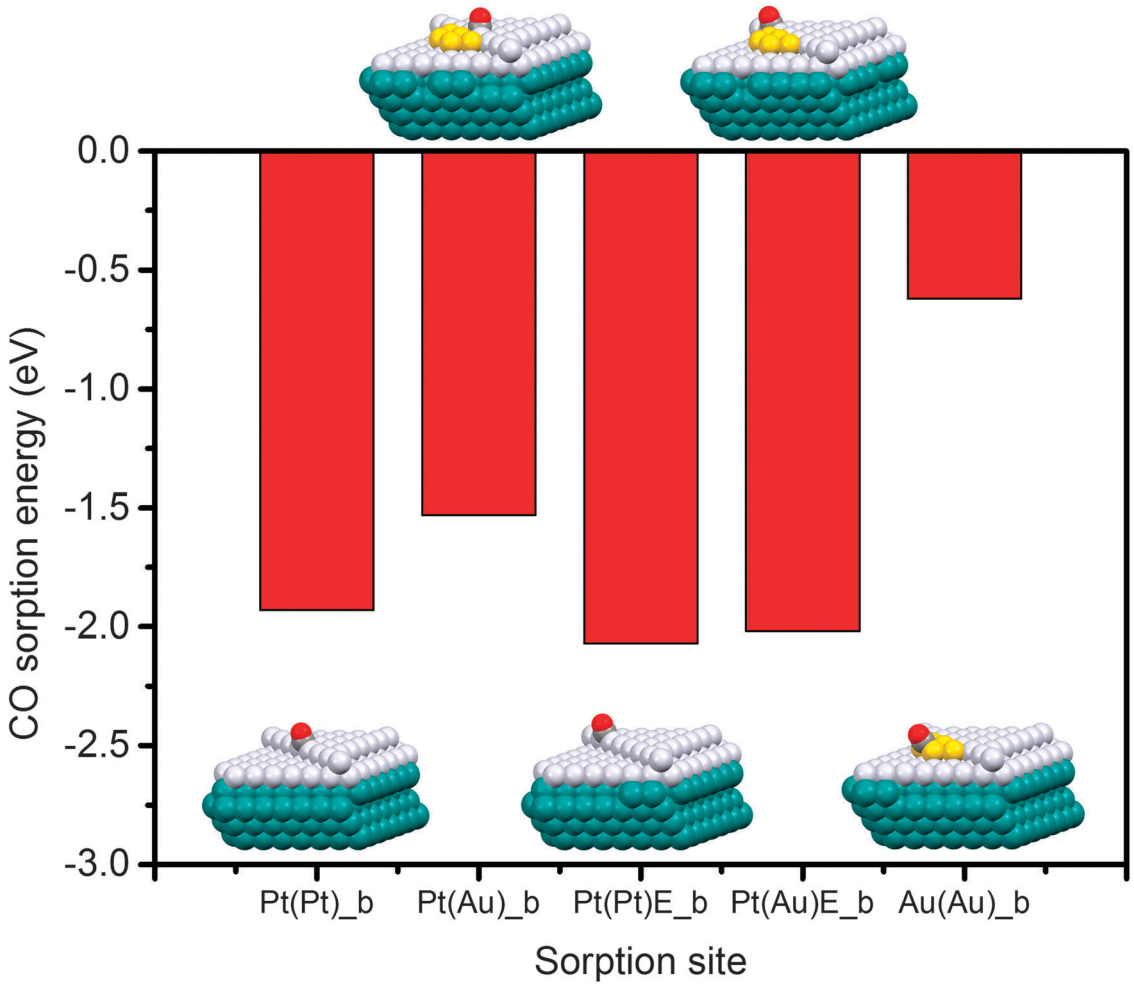

Fig. 4 DFT simulation of CO sorption model on 1.5 MLs of Pt atoms on the Ru(0001) facet with and without Au clusters in the kink region with the corresponding sorption energies.

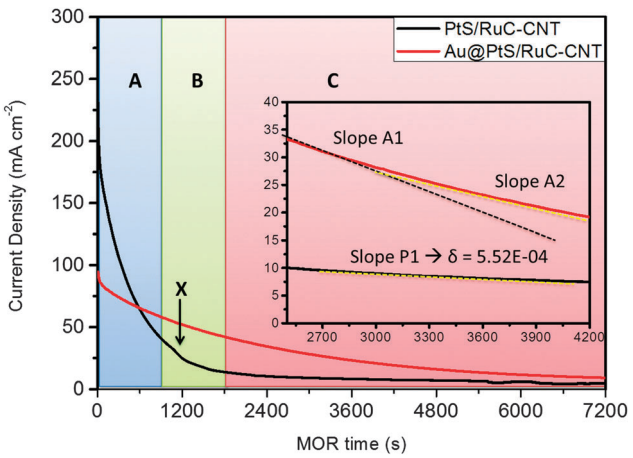

Fig. 5 Electrochemical spectra of two experimental NCs in a long-term MOR reaction (the inset shows line-fitting for the drop in current).

is found in region B, which suggests that corrosion due to protonation is substantially suppressed by the intercalation of Au clusters on Au@PtS/RuC.

The capability for CO tolerance of NCs can be illustrated by the rate of drop in current (δ) in region C on long-term MOR AC curves (see inset of Fig. 5) *via* a numerical representation:[18]

$$\delta = -\frac{100}{I_0} \times \left(\frac{\mathrm{d}I}{\mathrm{d}t}\right) (\% \ \mathrm{s}^{-1}) \qquad (3)$$

where I_0 and $\mathrm{d}I/\mathrm{d}t$ refer to the initial current density and the rate of drop in current in a short reaction period. Accordingly, the δ of PtS/RuC is determined to be -5.52×10^{-4}. It is interesting to note that the rate of drop in current has not stabilised at a constant value for Au@PtS/RuC (indicated by the different values of slope A1 and slope A2 at the beginning and end-point of AC in the inset). As consistently demonstrated by DFT simulations, this feature implies that the chemisorption kinetics between poisoning ligands (*i.e.*, OH and CO) and the reactant (MeOH) remain doubtful in this region, as the most active CO sorption sites (edge or bridge sites) were protected by Au atoms that were less poisoned by CO. Such unique characteristics rationalized the superior retention of current (2.5-fold) of Au@PtS/RuC compared to that of PtS/RuC in the MOR over 2 hours.

Our previous studies had demonstrated that lattice compression in the Pt-shell crystallite triggers electron injection

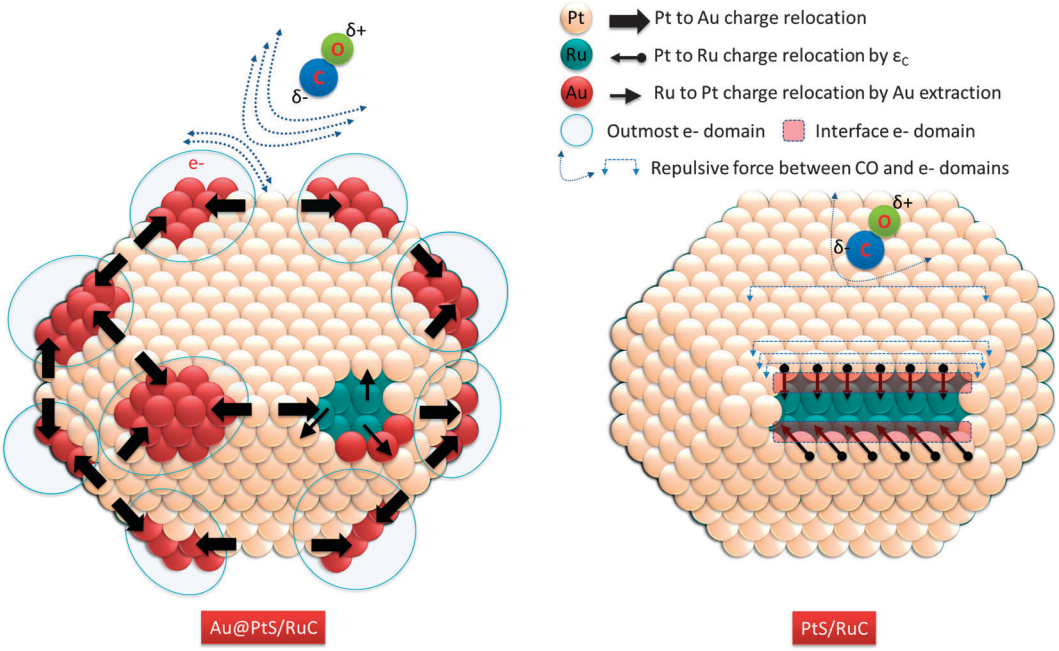

Scheme 1 Proposed atomic packing structure with corresponding electron relocation pathways on Ru-core/Pt-shell NCs with and without intercalation of sub-nanometer Au clusters. These Au clusters extract the valence charge from Pt and Ru crystallites to form a negatively charged shield that protects core–shell NCs from passivation by CO molecules.

from Pt to the sub-layer core crystal. As consistently shown by theoretical implications and analysis of VB spectra in the literature, this relocation of charge creates a negative-charge-rich domain at the interface (Scheme 1). This weakens the chemisorption bond of electronegative sorbates and therefore improves the chemical stability of NCs in electrochemical redox applications (for example, CO oxidation, MOR, DMFC, *etc.*). In this work, we demonstrate that such electron injection could be further enhanced and localized by Au clusters at an inter-facet corner (Scheme 1). These Au clusters trigger a strong local compressive strain in the Pt shell and extract certain electrons from the neighbouring Pt-shell crystal and even from the core crystal. This charge relocation pathway seems to contradict the well-studied practice of enhancing CO oxidation activity by applying lattice compression to a Pt-shell crystal.

However, this generates a localized electron charge field that creates an even stronger repulsive force to weaken the bonding of electronegative molecules (*e.g.*, chemisorption of CO) to the Au cluster and the neighbouring reaction sites. These electrochemical properties/hypotheses are consistently explained by combining results of the analysis of VB spectra and *ab initio* DFT simulations.[19,20] Accordingly, the external strain extracts electrons from Ru to Pt to the outermost band of NCs and leads to an upshift in the d-band centre of core–shell NCs.[9] Both of these features are consistent with the results of AC analysis and again promise outstanding tolerance for CO and electrochemical stability of Au@PtS/RuC.

Conclusions

A novel polyol redox method with sequential design was employed for intercalating Au clusters in the inter-facet regions of Ru-core/Pt-shell NCs. Our systematic structural characterizations in combination with theoretical simulations demonstrate that these gold clusters would tend to be located at the inter-facet corner sites of core–shell NCs. Such heterogeneous crystal growth is initiated by redox transmetallation nucleation followed by the thermal reduction of Au ions to a metallic crystal. These clusters truncate the inter-facet corners (reduce the surface defects) and grow into close-packed facets with small areas. In these circumstances, the stability for methanol electrooxidation of NCs was substantially improved. By combining DFT simulations and spectroscopic analyses, such stabilization originated from the prevention of surface oxidation and weakening of CO poisoning at Pt sites adjacent to the Au clusters. The former suppresses oxidation-assisted corrosion due to protonation (*i.e.*, reinforces the atomic structure) and the latter prolongs the MOR activity (prevents the reaction site Pt from being occupied by OH ligands or CO molecules) of Pt atoms in NCs. Both pathways are triggered by a localized strain field at the heterojunction between Au and the Pt shell. The heterojunction Au crystal covers dangling bonds and stabilizes the Pt atoms in the kink region. The local strain field in combination with a negative dipole extracts electrons from the core and the Pt shell to the Au clusters. Such extraction of charge passes the DOS on the outermost band of NCs. It forms a negatively charged field to expel highly electronegative ligands/molecules around the Au cluster and thus enhances the stability of NCs in the MOR. Most importantly, our results demonstrate a robust technique for surface modification (with fundamental understanding) to develop high-durability catalysts for long-term electrochemical reactions.

Acknowledgements

The authors would like to thank the staff of the National Synchrotron Radiation Research Center (NSRRC), Hsinchu, Taiwan for help in various synchrotron-based measurements. We appreciate the help from the National Center for High-Performance Computing (NCHC) of Taiwan for providing computational support. T.-Y. Chen acknowledges the funding support from research projects of the National Tsing Hua University, Taiwan (N103K30211 and 103N1200K3) and the Ministry of Science and Technology, Taiwan (MOST 103-2112-M-007 -022-MY3).

Notes and references

1 S. Goto, S. Hosoi, R. Arai, S. Tanaka, M. Umeda, M. Yoshimoto and Y. Kudo, *J. Phys. Chem. C*, 2014, **118**, 2634–2640.
2 K. Sasaki, H. Naohara, Y. Cai, Y. M. Chio, P. Liu, M. B. Vukmirovic, J. X. Wang and R. R. Adzic, *Angew. Chem., Int. Ed.*, 2010, **49**, 8602–8607.
3 S. Alayoglu, A. U. Nilekar, M. Mavrikakis and B. Eichhorn, *Nat. Mater.*, 2008, **7**, 333–338.
4 P. Strasser, S. Koh, T. Anniyev, J. Greeley, K. More, C. Yu, Z. Liu, S. Kaya, D. Nordlund, H. Ogasawara, M. F. Toney and A. Nilsson, *Nat. Chem.*, 2010, **2**, 454–460.
5 A. Schlapka, M. Lischka, A. Gross, U. Kasberger and P. Jakob, *Phys. Rev. Lett.*, 2003, **91**, 016101.
6 T. Bligaard and J. K. Nørskov, *Electrochim. Acta*, 2007, **52**, 5512–5516.
7 Y. Sun and Y. Xia, *Science*, 2002, **298**, 2176–2179.
8 T.-Y. Chen, T.-L. Lin, T.-J. M. Luo, Y. Chio and J.-F. Lee, *ChemPhysChem*, 2010, **11**, 2383–2392.
9 R. R. Adzic, J. Zhang, K. Sasaki, M. B. Vukmirovic, M. Shao, J. X. Wang, A. U. Nilekar, M. Mavrikakis, J. A. Valerio and F. Uribe, *Top. Catal.*, 2007, **46**, 249–262.
10 S. Alayoglu and B. Eichhorn, *J. Am. Chem. Soc.*, 2008, **130**, 17479–17486.
11 T.-Y. Chen, Y.-T. Liu, H.-S. Chen, K.-W. Wang, C.-T. Yang, T.-J. M. Luo, C.-H. Lee and T.-L. Lin, *CrystEngComm*, 2013, **15**, 3932–3942.
12 J. Teixeira, *J. Appl. Crystallogr.*, 1988, **21**, 781–785.
13 A. Guinier and G. Fournet, *Small-Angle Scattering of X-Rays*, John Wiley and Sons, New York, 1955.
14 J. Wagner, *J. Appl. Crystallogr.*, 2004, **37**, 750–756.
15 J. Greeley and M. Mavrikakis, *Nat. Mater.*, 2004, **3**, 810–815.
16 C.-C. Hu and K.-Y. Liu, *Electrochim. Acta*, 1999, **44**, 2727–2738.
17 C.-C. Hu and K.-Y. Liu, *Electrochim. Acta*, 2000, **45**, 3063–3068.
18 J. Jiang and A. Kucernak, *J. Electroanal. Chem.*, 2003, **543**, 187–199.
19 J.-J. Wang, Y.-T. Liu, I.-L. Chen, Y.-W. Yang, T.-K. Yeh, C.-H. Lee, C.-C. Hu, T.-C. Wen, T.-Y. Chen and T.-L. Lin, *J. Phys. Chem. C*, 2014, **118**, 2253–2262.
20 J. Ma, A. Habrioux, C. Morais, A. Lewera, W. Vogel, Y. Verde-Gómez, G. Ramos-Sanchez, P. B. Balbuena and N. Alonso-Vante, *ACS Catal.*, 2013, **3**, 1940–1950.